The influence of promoters (Zr, La, Tb, Pr) on the catalytic performance of CuO-CeO_2 systems for the preferential oxidation of CO in the presence of CO_2 and H_2O

Juan Antonio Cecilia[1], Ana Arango-Díaz[1], Verónica Rico-Pérez[2], Agustín Bueno-López[2], Enrique Rodríguez-Castellón[1]*

[1] Universidad de Málaga, Departamento de Química Inorgánica, Cristolografía y Mineralogía, Facultad de Ciencias, Campus de Teatinos, 29071 Málaga, Spain

[2] Universidad de Alicante, Departamento de Química Inorgánica, Ctra. San Vicente-Alicante, s/n, 03080 Alicante, Spain

Email: castellon@uma.es

Abstract

CuO supported on CeO_2 and $Ce_{0.9}X_{0.1}O_2$, where X is Zr, La, Tb or Pr, were synthesized using nitrate precursors, giving rise ceria based materials with a small particle size which interact with CuO species generating a high amount of interfacial sites. The incorporation of cations to the ceria framework modifies the CeO_2 lattice parameter, improving the redox behavior of the catalytic system. The catalysts were characterized by X-ray Diffraction (XRD), High-resolution Transmission Electron Microscopy (HRTEM), Raman spectroscopy, thermoprogrammed reduction with H_2 (H_2-TPR) and X-ray photoelectron spectroscopy (XPS). The catalysts were tested in the preferential oxidation of CO under a H_2-rich stream (CO-PROX), reaching conversion values higher than 95% between 115-140 ºC and being the catalyst with 6 wt.% of Cu supported on $Ce_{0.9}Zr_{0.1}O_2$ (sample 6CUZRCE) the most active catalyst. The influence of the presence of CO_2 and H_2O was also studied simulating a PROX unit, taking place a decreasing of the catalytic activity due to the inhibitor effect both CO_2 and H_2O.

Keywords: Copper oxide, cerium oxide, rare earth doped ceria, preferential CO oxidation, hydrogen

1. Introduction

In the last decades, new technologies have been developed for cleaner and more efficient energy production, and fuel cells have been pointed out as a promising alternative for this purpose. Among the several fuel cells available, the low-temperature proton exchange membrane fuel cell (PEMFC) has been largely studied in both mobile and stationary applications due to its high energy conversion at low temperature of operation (80 ºC) [1]. The H_2 used in the PEMFC is usually obtained by steam reforming, partial oxidation, or auto-thermal reforming of liquid hydrocarbons or natural gas in combination with the water gas shift (WGS) reaction. However, the H_2-rich stream coming from the WGS reaction exhibits CO concentration of about 1-2 vol. %. These values cannot be tolerated by the PEMFC because the catalytic anode is extremely sensitive to CO poisoning at concentrations higher than 10 ppm.

Several methods have been proposed to diminish the CO content of the H_2-rich stream. The main methods to remove the CO are as follows: i) Purification with a H_2 selective membrane, ii) CO methanation, iii) Pressure swing adsorption, and iv) Preferential oxidation of CO (CO-PROX). Among them, CO-PROX reaction has been considered as the straightforward and economical technique to minimize the CO content [2,3].

The CO-PROX catalysts must show high activity at the operating temperature of the fuel cells (80-120 ºC) with a good resistance to deactivation by H_2O and CO_2. Moreover CO-PROX catalysts need to be also highly selective towards the oxidation of CO, minimizing the consumption of H_2 by unwanted oxidation to water and avoiding the loss of energy [4].

Traditionally, noble-metal based catalysts with Pd [5], Rh [6,7], Ru [8,9] and mainly Au [10,11] and Pt [12-14] have shown to be active phases in the CO-PROX reaction. In spite of the high conversion values, the high cost and the availability of the noble metals limit its high scale application. This fact has led to the development of cheaper and more available active phases which show high activity and much higher selectivity to CO. The use of non-noble metal based catalysts, mainly copper catalysts, has received special attention due to the high selectivity in the CO-PROX reaction [15]. The use of ceria to form a $CuO\text{-}CeO_2$ system has been highly tested in the literature [16-22]. The establishment of intimate contact between CuO and CeO_2 generates a synergic effect that increases the catalytic activity, in which Cu^+ species are stabilized by

interaction between cooper oxide clusters and cerium oxide providing surface sites for easy CO adsorption [23].

Ceria is a key component in the catalytic system (CuO-CeO_2) due to the high ability to store and release oxygen [24]. Ceria exhibits two kinds of oxygen species available for its oxygen storage capacity (OSC), one being the surface oxygen and another the bulk oxygen. Besides limited bulk reducibility, pure ceria is associated with some other drawbacks like thermal sintering and deactivation of the Ce^{3+}/Ce^{4+} redox couple at high temperatures which result in the decline of OSC and catalytic activity. The doping of CeO_2 with isovalent/aliovalent cations can enhance the OSC, especially to improve the bulk reducibility at lower temperatures and to stabilize the structure against sintering [25].

The addition of isovalent cations as zirconium (Zr^{4+}) into the ceria framework increases the OSC by the formation of extrinsic oxygen vacancies that enhances the oxygen mobility by facilitating the Ce^{3+}/Ce^{4+} redox process, although the bulk oxygen mobility remains much less than the oxygen mobility at the surface [26]. The doping with aliovalent non-reducible cations such as lanthanum (La^{3+}) into the ceria framework enhances the OSC through the intrinsic oxygen vacancies [27]. The doping with variable valence cations into the ceria as terbium (Tb) and praseodymium (Pr) where coexist M^{3+} and M^{4+} oxidation states, (adopting M^{3+} oxidation state more easily than bulk ceria) [28], induces the formation of ordered intrinsic and extrinsic oxygen vacancies thereby enhance the OSC [29,30]. Despite of the doping is a key factor in the OSC, other factors can also influence the reducibility of ceria such as surface area, nature and distribution of dopant, oxygen vacancies and bulk oxygen mobility [31].

In the present research, a set of ceria based materials have been synthesized. These materials have been doped with isovalent cations such as zirconium, aliovalent non-reducible cations as lanthanum or variable valence cations as terbium or praseodymium which should provide diverse catalytic behavior to the ceria. These materials have been used as support of copper oxide to test the catalytic performance of this catalytic system in the CO-PROX reaction between 65 and 190 ºC. Moreover the influence of the CO_2 and H_2O in the feed, simulating a PROX unit fed with a H_2-rich H_2O- and CO_2-containing gas flow coming from a water-gas-shift reactor, was also evaluated.

2. Experimental

2.1. Catalyst preparation

CeO_2 and $Ce_{0.9}X_{0.1}O_2$ mixed oxides, where (*X* = Pr, Zr, La or Tb) were prepared by proper mixture of $Ce(NO_3)_3{\cdot}6H_2O$ (Aldrich 99.99%) and $Pr(NO_3)_3{\cdot}6H_2O$ (Aldrich 99.9%), $ZrO(NO_3)_2{\cdot}xH_2O$ (Aldrich), $La(NO_3)_3{\cdot}6H_2O$ (Aldrich 99.99%) or $Tb(NO_3)_3{\cdot}5H_2O$ (Aldrich 99.9%), respectively, to have a Ce:X molar ratio of 9:1. The mixture was calcined in a muffle furnace (in static air) from 25 to 500 ºC at 10 ºC min^{-1}, maintaining the sample at 500 ºC for 2 hours. Note that the stoichiometric coefficient of oxygen in $Ce_{0.9}X_{0.1}O_2$ could be lower than 2, mainly for mixed oxides containing +3 cations, but the coefficient 2 has been kept in the formula for the sake of simplicity.

Copper containing catalysts were prepared by incipient wetness impregnation of the supports with a solution of copper(II) acetate (6 wt.% Cu). After impregnation, the solids were dried overnight at 60 ºC and calcined during 4 h at 400 ºC. The catalysts were denoted 6CUXCE, where *X* is the doping agent added to the ceria.

2.2. Characterization methods

Powder patterns for the samples were collected on a X'Pert Pro MPD automated diffractometer (PANalytical B.V.) equipped with a Ge(111) primary monochromator (strictly monochromatic $CuK\alpha_1$ radiation) and an X'Celerator detector with a step size of 0.017º. The powder patterns were recorded between 10º and 70º in 2θ with a total measuring time of 30 min. Low angle measurements were obtained with the same configuration maintaining the divergence and anti-divergence aperture at 1/16º and with Soller of 0.02 rad. Measurements were carried out from 0.5-10° in 2θ with a step size of 0.017º. The particle size of CeO_2 and $Ce_{0.9}X_{0.1}O_2$ mixed oxides and the lattice strain were estimated by Williamson-Hall method with a fitting of the diffraction profile. The cell parameters were obtained from Rietveld method by using the X´Pert HighScore Plus software.

TEM micrographs of the catalysts were obtained with a Philips CM 200 Supertwin-DX4 high resolution transmission electron microscope. For sample preparation, a suspension of each catalyst was prepared and a drop of these suspensions was dispersed on a Cu grid.

H_2 temperature-programmed reduction (H_2-TPR) experiments were carried out to 0.080 g of catalyst previously treated with a He flow (35 ml min^{-1}) at 100 ºC for 30 min. After cooling to room temperature, the H_2 consumption was studied between this temperature and 800 ºC, by using an Ar/H_2 flow (48 ml min^{-1}, 10 vol. % of H_2) and under a heating rate of 10 ºC min^{-1}. Water formed in the reduction reaction was removed in an isopropanol-liquid nitrogen trap and a cold finger (−80 ºC). The H_2 consumption was measured with an on-line gas chromatograph (Shimadzu GC-14A) provided with a TCD. The H_2 consumed (TPR) was quantified by calibration with pure CuO as reference compound (Aldrich), assuming a total reduction of CuO to Cu^0.

X-ray photoelectron spectra were collected using a Physical Electronics PHI 5700 spectrometer with non-monochromatic Mg Kα radiation (300 W, 15 kV, and 1486.6 eV) with a multi-channel detector. Spectra of pelletized samples were recorded in the constant pass energy mode at 29.35 eV, using a 720 μm diameter analysis area. Charge referencing was measured against adventitious carbon (C 1*s* at 284.8 eV). A PHI ACCESS ESCA-V6.0 F software package was used for acquisition and data analysis. A Shirley-type background was subtracted from the signals. Recorded spectra were always fitted using Gaussian–Lorentzian curves in order to determine the binding energies of the different element core levels more accurately. Short irradiation time spectra of Cu 2*p* and C 1*s* were first registered to avoid as much as possible the photoreduction of Cu^{2+} species.

2.3. Catalytic tests

Catalytic tests were carried out in a fixed bed reactor at atmospheric pressure. The catalysts (0.150 g), with a particle size (0.050-0.110 mm) were introduced into a tubular stainless steel reactor (5 mm i.d.) with a thermocouple inside which is in contact with the catalysts. The samples were pre-treated in-situ under flowing air for 30 min at 400 ºC, followed by cooling to room temperature in He flow. The contact time W/F was 0.18 g s cm^{-3} (GHSV = 22000 h^{-1}). In most experiments, the reaction mixture composition was 1.25% CO, 1.25% O_2, 50% H_2, balanced with He. The effect of CO_2 and H_2O was examined with the addition of 15% CO_2 and 10% H_2O. An ice-salt cooled cold finger (-20 ºC) was used to trap the water downstream from the reactor. A Shimadzu-GC-2014 gas chromatograph equipped with TCD, with a CP-Carboplot-P7 column, was used to analyze the outlet composition. The detection limit for CO was 10 ppm. The temperature

was varied in the range of 65-190 ºC range, and measurements were carried out till a steady state was achieved.

The CO (Eq. (1)) and O_2 (Eq. (2)) conversions (x_{CO} and x_{O_2}, respectively) were calculated based on the CO and O_2 consumption, respectively:

$$x_{CO}(\%) = \frac{n_{CO}^{in} - n_{CO}^{out}}{n_{CO}^{in}} \times 100 \quad (1)$$

$$x_{O_2}(\%) = \frac{n_{O_2}^{in} - n_{O_2}^{out}}{n_{O_2}^{in}} \times 100 \quad (2)$$

where n_{CO}^{in} and n_{CO}^{out} are the inlet and outlet CO mole, respectively, and $n_{O_2}^{in}$ and $n_{O_2}^{out}$ are the counterpart O_2 mole.

The selectivity towards CO_2 was calculated by Eq. (3) [20,21]:

$$\mathrm{sel}_{CO_2}(\%) = \frac{1}{\lambda}\frac{x_{CO}}{x_{O_2}} \times 100 \quad (3)$$

where x_{CO} and x_{O_2} are the CO and O_2 conversions and λ is

$$\lambda = 2 \times \frac{n_{O_2}^{in}}{n_{CO}^{in}} \quad (4)$$

The excess of oxygen factor (λ) (Eq. (2) used was 2 because this value was previously found optimal for CO-PROX [20,21].

3. Results and discussion

3.1. Characterization of supports and fresh catalysts

3.1.1. X-ray diffraction

Figures 1A-B compiles the XRD patterns of the supports and fresh catalysts. Cerium oxide samples show broad diffraction peaks at 2Θ = 28.5, 33.4, 47.5 and 56.5º, which are assigned to CeO_2 with cubic fluorite-type structure (PDF Nº= 00-034-0394). CeO_2 doping produces slight shifts of the diffraction peaks, indicating the solid solution formation, where the cubic fluorite-type structure is maintained due to the relatively low content of doping agent. The incorporation of cations with different ionic radii than that of Ce^{4+} (see values in Table 1), smaller in the case of Tb^{4+} and Zr^{4+} and larger in the case

of La^{3+}, Tb^{3+} and Pr^{3+} provokes an increase of the ceria framework strain that leads to the modification of the cell parameters (Tables 2). Generally, the lattice parameter of the $Ce_{0.9}X_{0.1}O_2$ samples increases linearly with the ionic radii of the doping cation (Figure 2) due to the formation of a solid solutions with an expanded or contracted lattice.

In all cases the samples display a relatively small particle size in the range of 10-20 nm. Thus, the incorporation of small amounts of doping agents into the framework does not affect highly to the particle size of these ceria based materials (Table 2).

The addition of copper oxide into the cerium mixed oxides (Figure 1B and Table 2) seems neither affect the ceria lattice parameters nor the strain, revealing that copper oxide species were not incorporated into the ceria framework. However, the addition of copper species and the further calcination step provokes a slight increase of the particle size of CeO_2 samples, probably due to a sintering process. On the contrary, changes in the particle size of $Ce_{0.9}X_{0.1}O_2$ support are not obvious upon CuO loading, in line with the expected stabilizing effect of the dopants. The diffraction peaks attributed to copper species are not observed in most sample, except in the case of 6CULACE, where two noisy diffraction lines arise at 2Θ = 35.5 and 38.6º that are attributed to copper oxide (monoclinic tenorite) (PDF Nº: 00-048-1548). This fact confirms that copper oxide species present a small crystal size and that are well dispersed. It is expected that this type of dispersion generates a large amount of interfacial sites between $Ce_{0.9}X_{0.1}O_2$ and CuO where the CO-PROX reaction mainly takes place.

3.1.2. TEM Micrographs

High-Resolution Transmission Electron Microscopy (HRTEM) image (Figure 3) shows that the samples are formed by aggregates of crystals of about 15-20 nm of diameter, in agreement with the XRD data. In addition, small copper oxide crystallites grow over the lattice fringes of the ceria-based particles, corroborating the high dispersion of copper species. The interplanar distances of several crystals were determined. The larger distances correspond to (111) plane of the ceria-based supports. Unfortunately, it is difficult to differentiate between CuO and $Ce_{0.9}X_{0.1}O_2$ due to the similar d-spacing.

3.1.3. Raman spectroscopy

The Raman spectrum of CeO_2 (Figure 4A) shows a main band located at about 463 cm^{-1}, which is attributed to the F_{2g} vibrational mode of the cubic fluorite-type

structure of cerianite. Raman spectra of ceria-based oxides can potentially also display two weak bands located at 610 cm^{-1}, related to oxygen vacancies in the ceria lattice [32, 33] and at 245 cm^{-1}, assigned to the displacement of oxygen atoms from their ideal fluorite lattice position [34], and these features are observed in some Raman spectra of samples with doped ceria. $Ce_{0.9}Pr_{0.1}O_2$ and $Ce_{0.9}Tb_{0.1}O_2$ samples display a broad band located between 650 and 530 cm^{-1} assigned to non-degenerate Longitudinal Optical (LO) mode due to relaxation of symmetry rules. This is attributed to charge compensating defects induced by the incorporation of other metal cations into the ceria lattice generated by the formation of both extrinsic and intrinsic oxygen vacancies due to the incorporation of $Tb^{3+/4+}$ and $Pr^{3+/4+}$. This band grows significantly upon Pr or Tb doping due to the formation of more oxygen vacancies into the mixed oxide lattice in order to compensate the charge misbalance created by the presence of Pr^{3+} or Tb^{3+} cations [25,35].

In the case of $Ce_{0.9}Zr_{0.1}O_2$, the incorporation of zirconium into the ceria lattice improves the reducibility of ceria (see next section) but only creates few intrinsic oxygen vacancies. The replacement of Ce^{4+} by La^{3+} cations in the structure is also expected to produce oxygen vacancies to compensate the charge misbalance, although the vibrational mode at around 500-600 cm^{-1} is not well-defined in the Raman spectra of this sample, as has been reported previously in the literature [26,36].

Moreover, the doping of ceria provokes a shift of the F_{2g} vibrational mode in the Raman spectra. It has been reported in the literature that changes in the lattice parameters can affect the Raman peak position. Thus, the samples that suffer higher modifications in the CeO_2 lattice parameters present a higher shift in the Raman spectra [36,37], as is shown in Figure 5 where a relationship between the position of the F_{2g} band and the lattice parameter of the mixed oxide supports is evidenced.

The position of the F_{2g} vibrational mode obtained for the 6CUXCE catalysts (Figure 4B) shifts to lower wavenumbers by the formation of small proportion of CuO that shields to the ceria. It is worth to mention that bands located at 295, 340 and 626 cm^{-1} and attributed to the crystalline CuO are not observed in the Raman spectra of the catalysts, which confirms the high dispersion of the CuO species over the ceria based material [38].

3.1.4. H_2-TPR

The redox properties of the catalysts were evaluated by H_2-TPR measurements (Figure 6). It is well recognized in the literature that the CeO_2 reduction takes place in two steps. The first reduction step produces a maximum in the H_2-TPR profiles at about 530 ºC that is assigned to the reduction of surface cations. The second reduction step occurs at higher temperature, with a maximum at 900 ºC, and is ascribed to bulk reduction once the temperature is high enough for the bulk oxygen to be transported to the surface before the reduction [20]. With regards to the pure CuO, the reduction process occurs in a single step about 380 ºC.

The formation of CuO-CeO_2 system modifies the redox behavior of both CuO and ceria as a consequence of the CuO and CeO_2 interaction at the oxides interface [17, 20]. The reduction peaks are shifted to lower temperatures with regard to the reduction of the pure oxides, a broad band appearing at about 190 ºC. Different events take place within this band: CuO is reduced, H_2 is dissociated on Cu and hydrogen atoms spill over and reduces the ceria surface [34].

It has been reported [18, 20] that the doping of ceria with zirconium diminishes the reduction temperature compared to the pure ceria, reaching a maximum about 625 ºC. It is difficult to differentiate between the reduction attributed of surface and bulk oxygen due to both reduction peaks appear together by the easy reduction of the $Ce_{0.9}Zr_{0.1}O_2$. The isovalent substitution of Ce^{4+} by Zr^{4+}, that has a smaller cationic radii, generates oxygen vacancies favoring the oxygen mobility on the surface of the ceria. The presence of a higher amount of oxygen vacancies favors the reduction, and the temperature of 6CUZRCE reduction is shifted to lower temperature compared with 6CUCE (Figure 6), exhibiting a maximum about 160 ºC [20].

The doping of ceria with aliovalent non-reducible cations, such as La^{3+}, shifts the H_2 consumption peaks to lower reduction temperature with regard to ceria due to the diffusion of bulk oxygen to the surface creating more surface active sites for the adsorption of H_2 [26]. The incorporation of the CuO species leads to a redox couple that exhibits a similar behavior to that of 6CUCE.

The doping with variable valence cations into the ceria, such as those of terbium or praseodymium modifies the typical two-steps reduction of ceria. In the case of the terbium, its incorporation produces a modification of the ceria framework. Similarly to the ceria, the reduction of $Ce_{0.9}Tb_{0.1}O_2$ occurs in two steps. In the first step, the addition

of terbium species to CeO_2 provokes a shift of the reduction at lower temperature presumably due to the reduction of Tb^{4+} to Tb^{3+} together with the reduction of the oxygen located on the surface of the ceria. The second step, at about 700 ºC, is attributed to the reduction of the bulk oxide, which should be easier than for pure CeO_2,because of the distortion of the framework. The change of Ce^{4+} cations by Tb^{4+} cations, which have smaller atomic ratio, diminishes the cell volume and favors the reduction [28]. The incorporation of praseodymium into the ceria also shifts the reduction of the ceria towards lower temperature. The presence of high vacancies content produces a decrease of the bulk reduction [39]. The formation of the redox couple between CuO and the Pr-doped ceria also produces a decrease of the reduction temperature to 180-190 ºC.

It has been established in the literature that the H_2-TPR profiles of the CuO-CeO_2 based catalysts can be decomposed in three contributions [18]. The contribution at the lowest temperature, denoted as α peak, is assigned to the reduction of dispersed CuO in close contact with the CeO_2 surface. The second contribution, denoted as β peak, is attributed to CuO species highly dispersed and strongly interacting with CeO_2, and is typical of high copper content catalysts, and the third contribution at the highest temperature, denoted as γ peak, has been assigned to bulk copper oxide species which are associated with ceria. In all cases, the main H_2 consumption is attributed to the β peak which corroborates the high dispersion of the CuO species on the ceria surface.

Additionally to CuO reduction, surface ceria is simultaneously reduced in the broad H_2-TPR bands observed in Figure 6, and the presence of copper plays an important catalytic role. The H_2 consumption by the catalyst was quantified (Table 3), considering that the theoretical consumption of H_2 due to the reduction of all CuO in the samples is 755 μmol H_2 g^{-1}. In all samples the H_2 consumption is higher than the theoretical H_2 consumption required to reduce all copper (II) oxide species to Cu^0. This confirms that the reduction of copper oxide is overlapped by the simultaneous reduction of ceria.

3.1.5. X-ray photoloelectron spectroscopy (XPS)

In order to gain further insight into the surface composition of fresh catalysts, XPS spectra were analyzed. To avoid the photoreduction of both rare earths oxides and copper oxide, short irradiation times were used. Table 4 compiles the binding energies and redox parameters of the fresh catalysts.

Ce 3*d* core level spectra (Figure 7A and Table 4) can be decomposed in six contributions *v*, *u* (Ce $3d^9\ 4f^2$ O $2p^4$) and *v''*, *u''* (Ce $3d^9\ 4f^1$ O $2p^5$); *v'''*, *u'''* (final state of Ce $3d^9\ 4f^0$ O $2p^6$) assigned to that Ce^{4+} 3*d* final states and four contributions v_0,u_0 (Ce $3d^9\ 4f^2$ O $2p^5$) and *v'*, *u'* (Ce $3d^9\ 4f^1$ O $2p^6$) assigned to Ce^{3+} as a consequence of the hybridization between the Ce 4 levels and the O 2*p* states reveling that both Ce^{3+} and Ce^{4+}species are present in all catalysts [40].

The quantification of Ce^{3+} on the surface of the catalyst becomes necessary because Ce^{3+} and Cu^{2+} cations suffer a facile electron transfer by the synergetic effect between both species in the CO-PROX reaction. C3+ cuantification has been carried out with the formula:

$$Ce^{3+}(\%) = \frac{S(Ce^{3+})}{S(Ce^{3+} + Ce^{4+})} \text{ x } 100 = \frac{S(v) + S(u)}{S(v) + S(u) + S(v') + S(u')} \text{ x } 100$$

were $S(Ce^{x+})$ is the area of the deconvoluted peaks assigned to each cerium cations.

The profile of the Ce 3*d* core level spectra reveals the coexistence of both Ce^{3+} and Ce^{4+} species, although the main oxidation state is Ce^{4+} in all cases, and the Ce^{3+}/Ce^{4+} ratios obtained for all catalysts and supports are into the 0.03-0.12 range (see data in Table 4)

For the Cu 2*p* core level spectra (Table 2), the Cu $2p_{3/2}$ signal exhibits two contributions. The first band, located about 932.8 eV, is attributed to reduced copper species (Cu^0 and Cu^+) and the second one, centered at about 934.8 eV, is assigned to Cu^{2+} species. In addition, it is noticeable the presence of another band located about 942.1 eV attributed to the existence of a *shake-up* satellite peak typical of divalent species [20]. The presence of this band suggests that the main oxidation state of copper is 2+.

From the Cu $2p_{3/2}$ signal it is not possible to distinguish between the oxidation states Cu^0 and Cu^+. For this purpose, the Auger Cu LMM line (Figure 7B) was also analyzed, discerning two contributions centered about 916.3 eV and 917.8 eV and assigned to Cu^{2+} and Cu^+ species, respectively, where Cu^{2+} is the main contribution. The analysis of the ratio between the satellite peak and the main peak (I_{sat}/I_{main}) (Table 4) allows the estimation of the reduced copper species. I_{sat}/I_{main} ratio is in the range of 0.29-0.47 corroborating that copper species is mainly in the form of Cu^{2+}.

The Zr 3*d*, La 3*d*, Pr 3*d* and Tb 3*d* core level spectra were also evaluated, but are not shown for the sake of brevity. In the case of 6CUZRCE catalyst, Zr $3d_{5/2}$ core level spectrum shows a unique contribution located about 184.4 eV attributed to the presence of Zr^{4+} species. For 6CULACE catalyst, La $3d_{5/2}$ region exhibit a contribution about 834.6 eV assigned to La^{3+} species. Both Tb 3*d* and Pr 3*d* exhibit a similar behavior than was shown in Ce 3*d* core level spectra. It has been established in the literature the coexistence of both M^{3+} and M^{4+} oxidation states, located at 151.4 and 159.7 eV for the terbium and 929.6 eV and 934.5 eV for the praseodymium, respectively. Similarly to the Ce spectra, the main oxidation state both Tb and Pr are M^{4+}. Unfortunately, the Pr 3*d* spectrum cannot be resolved because of the overlapping of the Cu 2*p* and Pr 3*d* regions.

The O 1*s* core level spectra show an asymmetric peak that can be decomposed in two contributions at 529.0 and 531.1 eV assigned to the metal oxides and to carbonates or hydroxyls groups, respectively [20].

Finally, the C 1*s* core level spectra also exhibit two contributions located at 284.6 eV attributed to adventitious carbon and used as reference and another one located at 288.6 eV assigned to the presence of carbonates species, respectively.

3.2. Catalytic Results

The behavior of the 6CUXCE catalysts was evaluated in the CO-PROX reaction in a temperature range of 65-190 ºC. In all catalytic tests, both the reverse water gas shift and methanation reactions were found negligible under the reaction conditions used, and only the CO and H_2 oxidations are the reactions taking place.

3.2.1. CO-PROX reaction in CO +H_2 +O_2.

In all cases, the CO conversion, shown in Figure 8, increases with the reaction temperature reaching conversion values close to 100% at 115 ºC for 6CUZRCE, 6CUPRCE and 6CUTBCE catalysts and near to 95% at 140 ºC for 6CUCE and 6CULACE catalysts. According to Figure 8A profiles, the low temperature CO oxidation activity follows the trend:

6CUZRCE > 6CUPRCE ≈ 6CUTBCE > 6CUCE > 6CULACE

This trend suggests that the effect of the ceria dopant is related to the charge of the foreign cation, 4+ cations being better than 3+ cations, that is, the best performance is obtained with Zr^{4+}, followed by $Pr^{4+/3+}$ and $Tb^{4+/3+}$, and finally La^{3+}. This could be tentatively attributed to the effect of the dopant on the stability of chemisorbed CO_2 species formed as CO oxidation product. It is expected that such chemisorbed CO_2 species are more stable on 3+ cations than on 4+ cations, because CO_2 is an acid gas and, as a general trend, 3+ cations are expected to be more basic than 4+ cations (this would be definitively the case for cations with the same size). According to this, the poisoning effect of the surface CO_2 species formed as reaction product would be the main argument to explain the observed catalytic activity trend. Additional information about this hypothesis is obtained in the next section, where the effect of CO_2 in the fed is discussed.

In addition, the best catalytic activity for low temperature CO oxidation of 6CUZRCE could be also related to the easiest reducibility of this catalyst, as deduced from the lowest reduction temperature observed in H_2-TPR profiles (see Figure 6). If Zr^{4+} doping decreases the catalyst reducibility in H_2-TPR experiments, it is not surprising the same behavior to occur by reduction with CO in PROX experiments. However, this do not applies to all catalyst, suggesting that the effect of the chemisorbed CO_2 stability prevails.

With regards to the CO selectivity towards CO_2, all catalysts exhibit high selectivity values at 65 ºC which decrease progressively with temperature due to H_2 oxidation, as expected [41]. Differences in selectivity among catalysts are minor under the experimental conditions used in Figure 8 experiments.

3.2.2. CO-PROX reaction in CO +H_2 +O_2 +CO_2.

The influence of the CO_2 in the feed was studied including this gas in the reaction mixture, and the profiles obtained are compiled in Figure 9.

The presence of CO_2 in the gas stream provokes a shift of CO conversion to higher reaction temperature (compare curves in Figures 8 and 9, temperatures for 50% CO convension in Table 1 of the supplementary information), reaching the highest conversion values between 140 and 165 ºC. The CO conversion follows a quite similar trend to that observed in previous experiments performed without CO_2 in the feed.

6CUZRCE > 6CUPRCE > 6CUTBCE > 6CUCE > 6CULACE

Ceria doping with 4+ cations provides better activity than doping with 3+ cations also in experiments performed with CO_2 in the fed, that is, the best performance is obtained with Zr^{4+} and the worst with La^{3+}. Comparison of Figures 8 and 9 suggest that, in spite of all catalysts decrease their CO oxidation capacity in the presence of CO_2, 6CULACE suffers the strongest decrease. This supports our previous hypothesis, that is, the basic 3+ dopants like La^{3+} are expected to stabilize CO_2-like species on surface stronger than the more acid 4+ cations, and the desorption of CO_2 molecules requires an increase in temperature to get the catalyst active sites available for the CO-PROX reaction [42].

It is interesting to analyze in detail the effect of CO_2 in the performance the 6CUPRCE and 6CUTBCE catalysts. Both Pr and Tb are able to adopt 3+ and 4+ oxidation states, as previously mentioned, and the behavior of 6CUPRCE and 6CUTBCE is equal in experiments performed with CO_2 in the fed (Figure 8). However, 6CUTBCE suffers a stronger deactivation when CO_2 is included in the fed than 6CUPRCE, and this could be related to the easier low temperature reducibility observed in H_2-TPR experiments. The lowest temperature H_2 consumption peak in Figure 5 suggests that 6CUTBCE is reduced slightly better at such lowest temperature than 6CUPRCE, and this would lead to the formation of more Tb^{3+} cations than Pr^{3+} cations under CO-PROX conditions, therefore being more prone to deactivation by CO_2 poisoning.

3.2.3. CO-PROX reaction in CO +H_2 +O_2 +CO_2 +H_2O.

The influence of the presence of both CO_2 and H_2O in the feed was also tested including 15 vol. % CO_2 and 10 vol. % H_2O in the gas stream (Figure 10). As expected, the presence of CO_2 and H_2O in the gas stream decreases the activity of all catalysts (Compare Figures 8, 9 and 10 and temperatures for 50% CO conversion in the Table 1 of the supplementary information). It is known that H_2O hinders the access of the CO molecules to the interfacial CuO-Ceria sites [43]. This fact, together with the competitive effect between CO and CO_2 molecules by the active centers, leads to the CO conversion curves delay reaching the maximum conversion values (between 80-95%) at 140 ºC for all catalysts.

The catalytic results obtained in this complex reaction mixture (Figure 10) reveal that the performance of all catalysts is not as different as previously observed in the absence of H_2O (Figures 8 and 9), and this suggests that the presence of H_2O in somehow

affects the poisoning effect of CO_2 either in the fed (Figure 9) or formed as CO oxidation product (Figure 8). For instance, the 6CULACE catalyst showed the worst catalytic activity for CO oxidation in the absence of H_2O, while its performance in the presence of H_2O is similar to that of the remaining catalysts. This could mean that the poising effect of H_2O prevails and masks the effect of CO_2 poisoning and/or that H_2O hinders CO_2 poisoning affecting each catalyst in a different way depending on its ability for CO_2 chemisorption.

3.3. Characterization of used catalysts

In order to evaluate potential changes on the catalysts during the catalytic test, the used catalysts were recovered after the catalytic process and analyze by XRD and XPS.

In all cases, the X-ray diffractograms of the used catalysts do not show noticeable changes in the crystallinity of the ceria during the catalytic test (Figure 11). In the same way, both the lattice parameters and the strain remain unaltered revealing that the ceria presents a high stability (Table 5). Copper oxide species, which was highly dispersed in the fresh catalysts, disappears after the catalytic test, arising new diffraction peaks more defined at 2Θ (º) = 43.5 and 50.4 associated to Cu^0 (PDF 00-004-0836) due to the H_2-rich stream employed in the CO-PROX reaction which corroborates the sintering of the copper species. The formation of Cu^0 species provokes the loss of the redox couple CeO_2-CuO leading to a decreasing of the number of the interfacial sites, where are located the active sites of the reaction, as a consequence of catalytic deactivation.

XPS spectra of the used catalysts show in the Ce 3*d* region (Figure 12A) how the catalysts maintain a low photoreduction degree. Similarly, La 3*d*, Zr 3*d*, Pr 3*d* and Tb 3*d* regions preserve their oxidation states after the catalytic test, which confirms the high stability of the ceria mixed oxides materials (Table 4). With regards to the Cu 2*p* core level spectra (Figure 12B), the intensity of the satellite *shake-up* decreases after the catalytic test in all cases due to the H_2-rich feed used in the reaction which suggests the formation of reduced copper species corroborating the XRD data of the spent catalysts (Figure 11).

4. Conclusions

$Ce_{0.9}X_{0.1}O_2$ samples have been synthesized using nitrate species as precursors, and it has been evaluated the influence of the nature of the doping species in the physichemical properties of these mixed oxides.. These materials were used as support of CuO and were evaluated in the CO-PROX reactionand conversion values higher than 95% were obtained between 115-140 ºC, being 6CUZRCE the most active catalyst. The catalytic activity of the CuO/Ceria catalysts evaluated seems to be related to the charge of the doping cations, +4 cations providing better performances than +3 cations.

In addition, it was evaluated the influence of CO_2 and CO_2 + H_2O in the feed stream, simulating a PROX unit operation where the effluent comes from a water-gas-shift reactor. The catalytic results reveal a decrease in the catalytic activity due to an inhibitor effect in both cases due to the competitive CO, CO_2 and H_2O chemisorption on the active sites.

The analysis of the used catalyst reveals the reduction of the proportion of copper oxide species during the PROX reaction. The XPS measurements of the used catalysts show how both CeO_2 and $Ce_{0.9}M_{0.1}O_2$ maintain a similar behavior which confirms the high stability of these materials.

Acknowledgments

The projects CTQ2012-37925-C03-03 and CTQ2012-30703 of Ministerio de Economía y Competitividad (Spain), the project of Excellence P12 RNM 1565 (Junta de Andalucía, Spain), the project of Excellence PROMETEUII/2014/010,(Generalitat Valenciana) and the UE (FEDER funding) are acknowledged for the financial support.

Tables

Table 1. Ionic radii of cations present in the ceria-based supports.

Element	**Ionic radii (Å)**	
	M^{4+}	**M^{3+}**
Ce	0.97	1.14
Zr	0.84	-
La	-	1.10
Tb	0.88	1.04
Pr	0.96	1.13

Table 2. XRD characterization results of the supports and fresh catalysts.

Samples	CeO_2 Crystal size (nm)	CeO_2 Strain	CeO_2 lattice parameter(a/Å)	Disagreement factor (R_{wp}) (%)
Support				
CeO_2	10.4	0.236	5.415	9.90
$Ce_{0.9}Zr_{0.1}O_2$	13.0	0.543	5.412	7.70
$Ce_{0.9}La_{0.1}O_2$	20.0	0.629	5.445	7.48
$Ce_{0.9}Tb_{0.1}O_2$	13.7	0.694	5.407	7.75
$Ce_{0.9}Pr_{0.1}O_2$	18.0	0.614	5.419	7.16
Fresh Catalysts				
6CUCE	36.7	0.148	5.411	5.77
6CUZRCE	14.0	0.634	5.410	5.02
6CULACE	20.2	0.609	5.443	5.38
6CUTBCE	16.8	0.552	5.423	6.07
6CUPRCE	13.7	0.659	5.411	5.12

Table 3. Reducibility degree for 6CUXCE catalyts obtained by H_2-TPR.

Sample	$T_{R(MAX)}$ (ºC)	Peak *α* (%)	Peak β (%)	Peak γ (%)	β+γ	α/(β+γ)	H_2 consumed* (µmol g^{-1})	H_2/Cu
6CUCE	191	30	64	6	70	0.43	953	1.26
6CUZRCE	157	15	65	20	79	0.18	832	1.10
6CULACE	170	21	48	31	79	0.27	1104	1.46
6CUTBCE	184	26	66	8	74	0.35	938	1.24
6CUPRCE	185	39	54	7	61	0.64	990	1.31

*The expected amount H_2 consumed by CuO reduction, considering the CuO loading, is 755 µmol H_2 g^{-1}

Table 4. Binding energies and redox parameters of fresh and used catalysts.ng energies and redox parameters of fresh

Sample	Cu $2p_{3/2}$ (eV)	Cu_{red}/CuO	I_{Sat}/I_{pp}	Ce^{3+}/Ce^{4+}	Cu/(Ce+X)	X/Ce
Fresh Catalysts						
6CUCE	931.7 (34.6%) 933.3 (65.4%)	0.35	0.29	0.08	0.45	0
6CUZRCE	932.7 (30.2%) 934.4 (69.8%)	0.30	0.33	0.12	0.39	0.08
6CULACE	931.8 (29.2%) 933.0 (70.9%)	0.29	0.44	0.11	0.37	0.14
6CUTBCE	931.9 (27.5%) 933.2 (72.5%)	0.28	0.47	0.08	0.33	0.18
6CUPRCE	-	-	-	0.08	0.75	0.13
Used Catalysts						
6CUCE-U	932.9 (45.0%) 934.6 (55.0%)	0.45	0.36	0.03	1.03	0
6CUZRCE-U	932.1 (34.8%) 934.1 (65.2%)	0.35	0.40	0.08	0.48	0.08
6CULACE-U	932.4 (79.2%) 934.3 (20.8%)	0.79	0.30	0.06	0.60	0.10
6CUTBCE-U	931.2 (34.8%) 933.4 (80.7%)	0.39	0.34	0.07	0.67	0.09
6CUPRCE-U	-	-	-	0.08	0.46	0.08

X = Zr, Pr, Tb or La.

Table 5. XRD characterization results of the used catalysts.

Samples	CeO_2 Particle size (nm)	CeO_2 Strain	CeO_2 lattice parameter(a/Å)	CeO_2 (%) wt.	Disagreement factor (R_{wp}) (%)
Used Catalysts					
6CUCE-U	27.5	0.107	5.412	96.8	5.59
6CUZRCE-U	10.2	0.541	5.411	95.9	4.76
6CULACE-U	18.5	0.600	5.444	96.7	5.01
6CUTBCE-U	17.5	0.603	5.427	97.1	5.37
6CUPRCE-U	13.3	0.662	5.412	97.8	5.13

Supplementary information (Table 1). Temperature for 50% CO conversion.

Catalytic activity T_{50} (ºC)					
Catalytic test	**6CUCE**	**6CUZRCE**	**6CULACE**	**6CUTBCE**	**6CUPRCE**
Elementary test	92	67	99	75	77
CO_2	119	93	150	100	109
CO_2 +H_2O	117	122	127	122	134

Figure captions.

Figure 1. XRD patterns of supports (A) and 6CUXCE catalysts (B).

Figure 2. Relationship between lattice parameter of the mixed oxide supports and ionic radii of the doping cation.

Figure 3.

Figure 4. Raman spectra of supports (A) and 6CUXCE catalysts (B).

Figure 5. Relationship between the position of the F_{2g} band and lattice parameter of the mixed oxide supports.

Figure 6. H_2-TPR profiles of 6CUXCE catalysts.

Figure 7. Ce 3*d* core level spectra (A) and Auger Cu LMM line (B) of 6CUXCE catalysts.

Figure 8. CO conversion (A) and selectivity toward CO_2 (B) as function of the temperature of 6CUMCE catalysts. Operating conditions: GHSV = 22,000 h^{-1}, λ = 2, 1.25% CO, 1.25 %O_2, 50% H_2, He balance (%vol).

Figure 9. CO conversion (A) and selectivity toward CO_2 (B) as function of the temperature of 6CUMCE catalysts. Operating conditions: GHSV = 22,000 h^{-1}, λ = 2, 1.25% CO, 1.25 %O_2, 50% H_2, 15% CO_2, He balance (%vol).

Figure 10. CO conversion (A) and selectivity toward CO_2 (B) as function of the temperature of 6CUMCE catalysts. Operating conditions: GHSV = 22,000 h^{-1}, λ = 2, 1.25% CO, 1.25 %O_2, 50% H_2, 15% CO_2, 10% H_2O, He balance (%vol).

Figure 11. XRD of fresh and spent catalysts of 6CUXCE catalysts.

Figure 12. Ce 3*d* core level spectra (A) and Auger Cu LMM line (B) of used 6CUXCE catalysts.

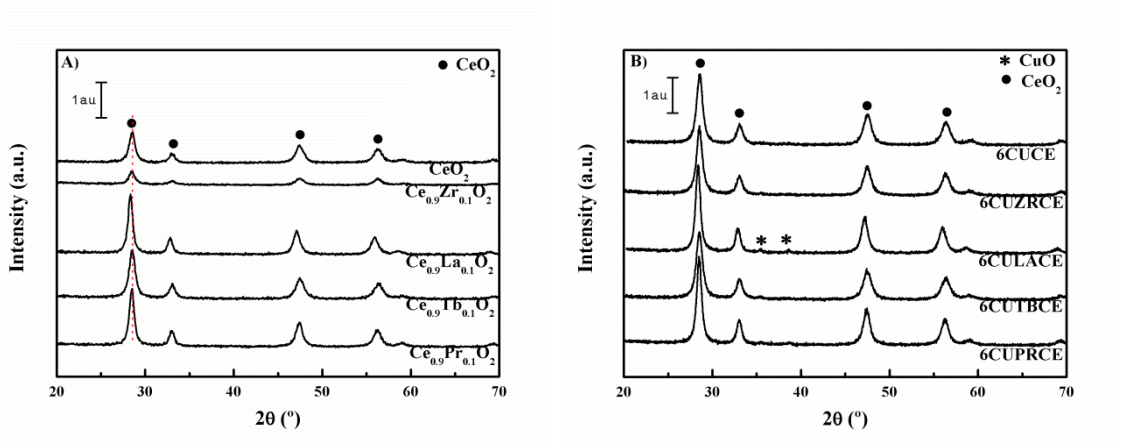
A)
● CeO2
1au
CeO2
Ce0.9Zr0.1O2
Ce0.9La0.1O2
Ce0.9Tb0.1O2
Ce0.9Pr0.1O2
Intensity (a.u.)
20
30
40
50
60
70
2θ (°)
B)
* CuO
● CeO2
1au
6CUCE
6CUZRCE
6CULACE
6CUTBCE
6CUPRCE
Intensity (a.u.)
20
30
40
50
60
70
2θ (°)

Figure 1

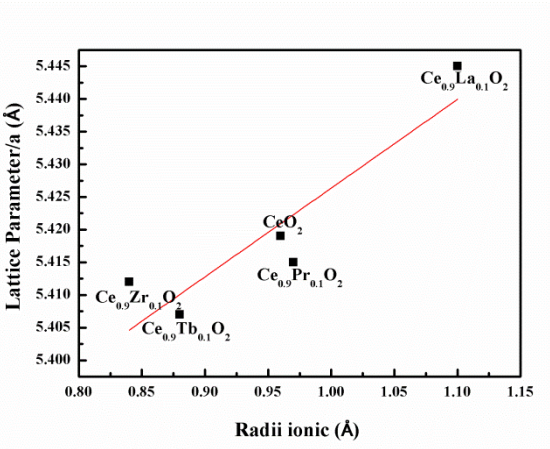
Lattice Parameter/a (Å)
5.445
5.440
5.435
5.430
5.425
5.420
5.415
5.410
5.405
5.400
0.80
0.85
0.90
0.95
1.00
1.05
1.10
1.15
Radii ionic (Å)
Ce0.9La0.1O2
CeO2
Ce0.9Pr0.1O2
Ce0.9Zr0.1O2
Ce0.9Tb0.1O2

Figure 2

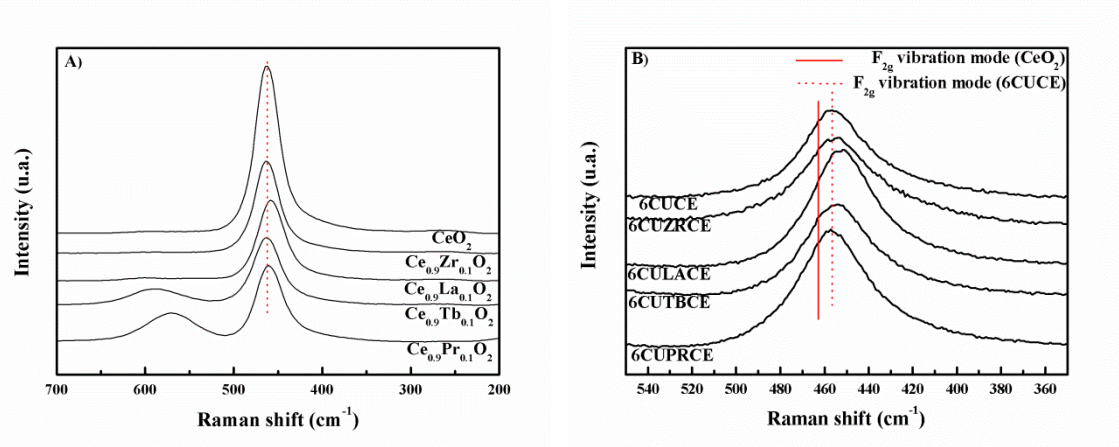
A)
Intensity (u.a.)
CeO2
Ce0.9Zr0.1O2
Ce0.9La0.1O2
Ce0.9Tb0.1O2
Ce0.9Pr0.1O2
700
600
500
400
300
200
Raman shift (cm-1)
B)
F2g vibration mode (CeO2)
F2g vibration mode (6CUCE)
Intensity (u.a.)
6CUCE
6CUZRCE
6CULACE
6CUTBCE
6CUPRCE
540
520
500
480
460
440
420
400
380
360
Raman shift (cm-1)

Figure 4

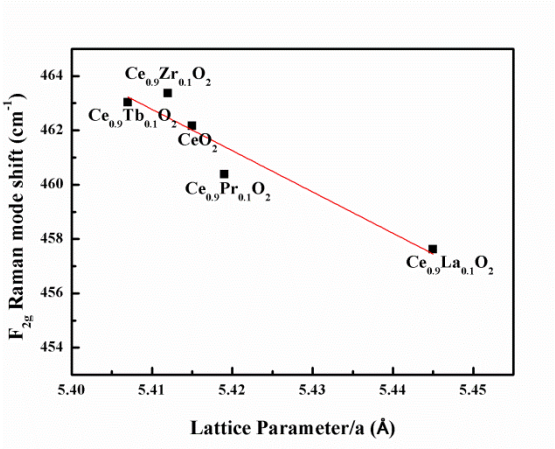
Ce0.9Zr0.1O2
Ce0.9Tb0.1O2
CeO2
Ce0.9Pr0.1O2
Ce0.9La0.1O2
F2g Raman mode shift (cm-1)
Lattice Parameter/a (Å)
464
462
460
458
456
454
5.40
5.41
5.42
5.43
5.44
5.45

Figure 5

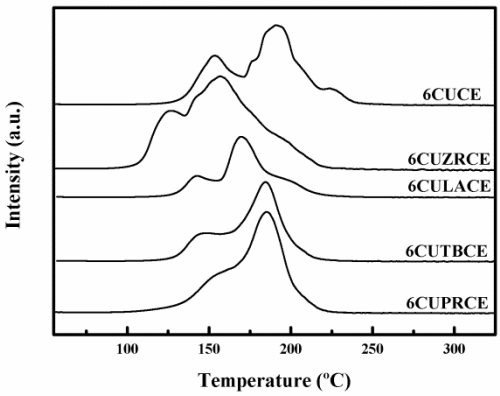
Intensity (a.u.)
6CUCE
6CUZRCE
6CULACE
6CUTBCE
6CUPRCE
100
150
200
250
300
Temperature (°C)

Figure 6

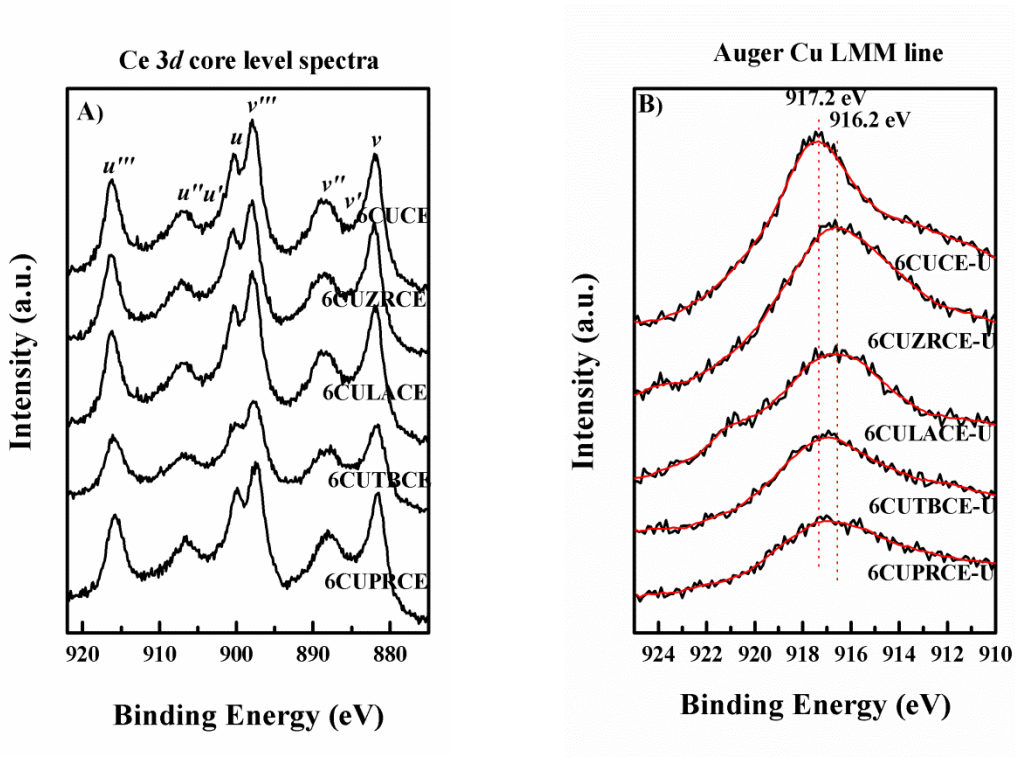
Ce 3d core level spectra
A)
u'''
u''u'
u
v'''
v''
v'
v
6CUCE
6CUZRCE
6CULACE
6CUTBCE
6CUPRCE
Intensity (a.u.)
920
910
900
890
880
Binding Energy (eV)
Auger Cu LMM line
B)
917.2 eV
916.2 eV
6CUCE-U
6CUZRCE-U
6CULACE-U
6CUTBCE-U
6CUPRCE-U
Intensity (a.u.)
924
922
920
918
916
914
912
910
Binding Energy (eV)

Figure 7

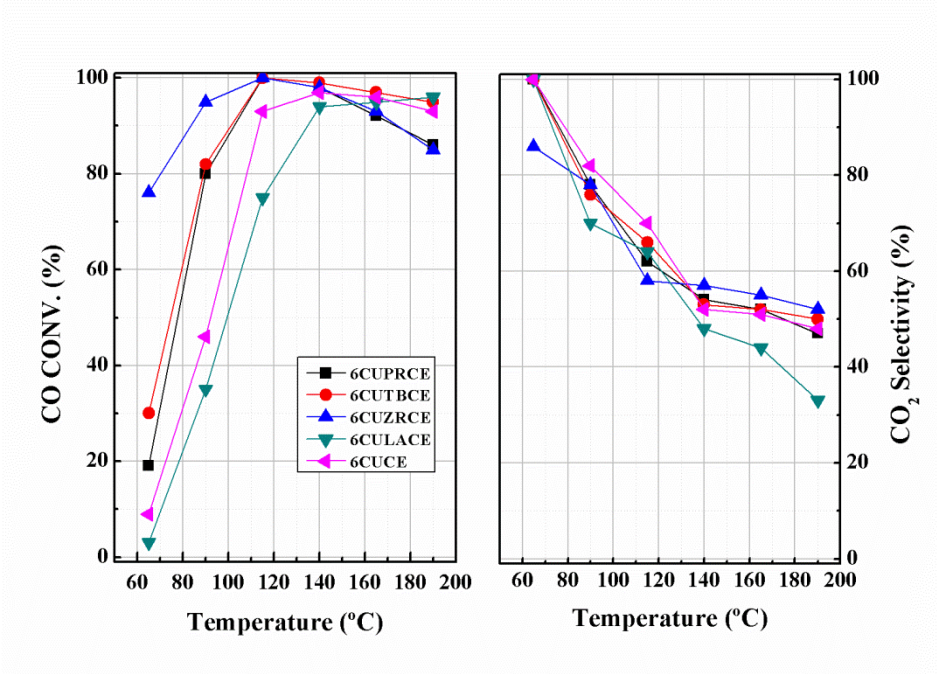
CO CONV. (%)
Temperature (°C)
6CUPRCE
6CUTBCE
6CUZRCE
6CULACE
6CUCE
CO2 Selectivity (%)
Temperature (°C)

Figure 8

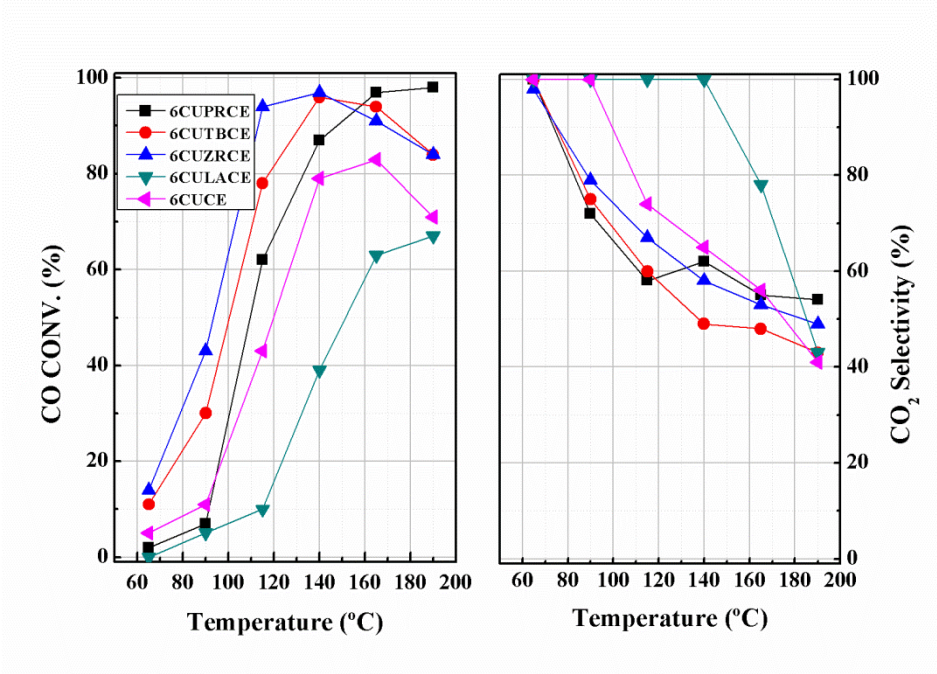
6CUPRCE
6CUTBCE
6CUZRCE
6CULACE
6CUCE
CO CONV. (%)
Temperature (°C)
CO2 Selectivity (%)
Temperature (°C)

Figure 9

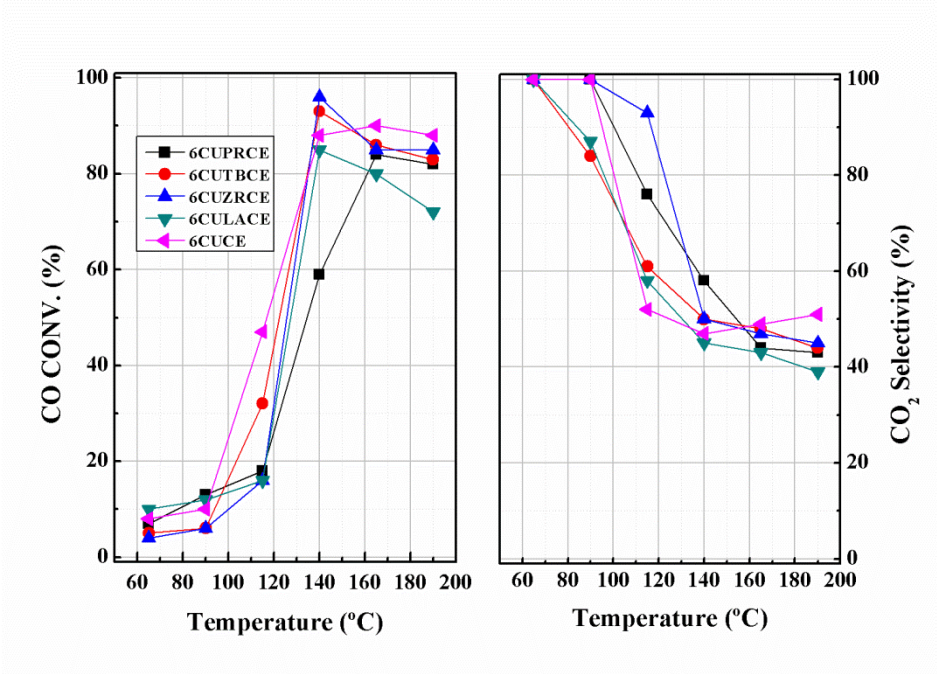
6CUPRCE
6CUTBCE
6CUZRCE
6CULACE
6CUCE
CO CONV. (%)
Temperature (°C)
CO2 Selectivity (%)
Temperature (°C)

Figure 10

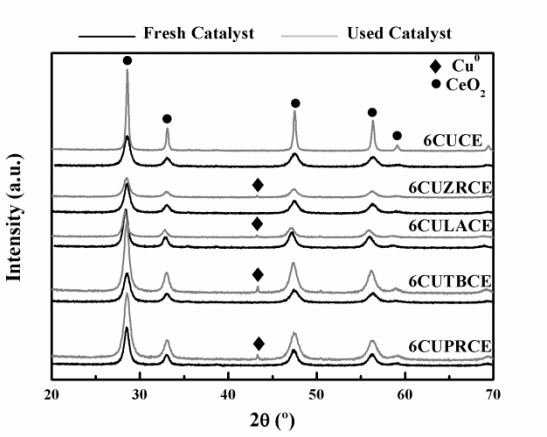
Fresh Catalyst
Used Catalyst
Cu0
CeO2
6CUCE
6CUZRCE
6CULACE
6CUTBCE
6CUPRCE
Intensity (a.u.)
20
30
40
50
60
70
2θ (°)

Figure 11

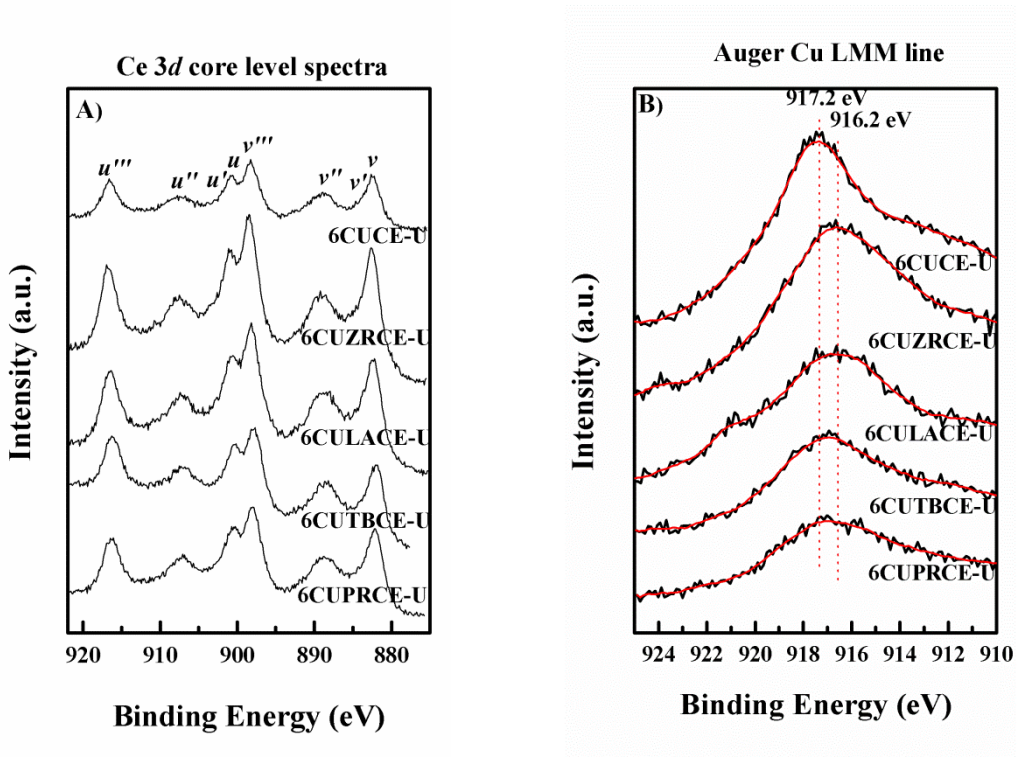
Ce 3d core level spectra
A)
u'''
u''
u'
u
v'''
v''
v'
v
6CUCE-U
6CUZRCE-U
6CULACE-U
6CUTBCE-U
6CUPRCE-U
Intensity (a.u.)
920
910
900
890
880
Binding Energy (eV)
Auger Cu LMM line
B)
917.2 eV
916.2 eV
6CUCE-U
6CUZRCE-U
6CULACE-U
6CUTBCE-U
6CUPRCE-U
Intensity (a.u.)
924
922
920
918
916
914
912
910
Binding Energy (eV)

Figure 12

REFERENCES

[1] M.P Woods, P. Gawade, B. Tan, U.S. Ozkan, Appl. Catal. B: Environ. 97 (2010) 28-35.
[2] J.D. Morse, Int. J. Energy Res. (31) 2007 576-602.
[3] A. Mishra, R. Prasad, B Chem. React. Eng. Catal. 6 (2011) 1-14.
[4] N. Bion, F. Epron, M. Moreno, F. Mariño, D. Duprez, Top. Catal. 51 (2008) 76-88.
[5] O. Pozdnyakova, D. Teschner, A. Wootsch, J. Kröhnert, B. Steinhauer, H. Sauer, L. Toth, F.C. Jentoft, A. Knop-Gericke, Z. Paál, R. Schlögl, J. Catal. 237 (2006) 17-28.
[6] C. Galletti, S. Specchia, G. Saracco, V. Specchia, Ind. Eng. Chem. Res. 47 (2008) 5304-5312.
[7] S. Ito, H. Tanaka, Y. Minemura, S. Kameoka, K. Tomishige, K. Kunimori, Appl. Catal. A: Gen. 273 (2004) 295-302.
[8] Y.F. Han, M.J. Kahlich, M. Kinne, R.J. Behm, Phys. Chem. Chem. Phys. 4 (2002) 389-397.
[9] L. Wang, J. Chen, A. Patel, V. Rudolph, Z. Zua, Appl. Catal A: Gen. 447-448 (2012) 200-209.
[10] L. Ilieva, G. Pantaleo, I. Ivanov, R. Zanella, A.M. Venezia, D. Andreeva, Int. J. Hydrogen. Energ. 34 (2009) 6505-6515.
[11]. Ilieva, P. Petrova, T. Tabakova, G. Pantaleo, V. Montes , J.W. Sobczak , W. Lisowski, Z. Kaszkur, M. Boutonnet, A.M. Venezia, Fuel 134 (2014) 628-635.
[12] J.L. Ayastuy, A.Gel-Rodríguez, M.P. González-Marcos, M-P. Gutiérrez-Ortíz, Int. J. Hydrogen. Energ. 31 (2006) 2231-2242.
[13] M. Souza, N. Ribeiro, M. Schmal, Int. J. Hydrogen Energ. 32 (2007) 452-429.
[14] M. Kuriyama, H.S. Tanaka, I. Ito, T. Kubota, T. Miyao, S. Naito, K. Tomishige, K. Kunimori, J. Catal. 225 (2007) 39-48.
[15] S. Kandoi, A.A. Gokhale, L.C. Grabow, J.A. Dumesic, M Mavrikakis, Catal. Lett. 93 (2004) 93-100.
[16] D. Gamarra, A. Hornés, Z. Koppány, G. Munuera, J. Soria, A. Martínez-Arias, J. Power Sources 169 (2007) 110-116.
[17] A. Martínez-Arias, A.B. Hungría,. G. Munuera, D. Gamarra, Appl. Catal. B. Environ. 65 (2006) 207-216.
[18] J.L. Ayastuy, A. Gurbani, M.P. González- Marcos, M.A. Gutiérrez-Ortíz, Int. J. Hydrogen Energ. 35 (2010) 1232-1244.
[19] A. Gurbani, J.L. Ayastuy, M.P. González-Marcos, M.A. Gutiérrez-Ortíz, Int. J. Hydrogen Energ. 35 (2010) 11582-11590.
[20] A. Arango-Díaz, J.A. Cecilia, E. Moretti, A. Talon, P. Núnez, J. Marrero-Jerez, J. Jiménez-Jiménez, A. Jiménez-López, Int. J. Hydrogen Energ. 39 (2014) 4102-4108.
[21] E. Moretti, L. Storaro, A. Talon, R. Moreno-Tost, E. Rodríguez-Castellón, A. Jiménez-López, M. Lenarda, Catal. Lett. 129 (2009) 323-336.
[22].T. Caputo,L. Lisi, R. Pirone, G. Russo, Appl. Catal. A: Gen. 348 (2008) 42-53.
[23] A. Martínez-Arias, M. Fernández-García, J. Soria, J. C. Conesa, J. Catal. 182 (1999) 367-377.
[24] J. Kaspar, M. Graziani, P. Fornasiero, *Handbook on the Physics and Chemistry of Rare Earths*, 29 (2000) 159-267.
[25] B.M. Reddy, G. Thrimurthulu, L. Katta, Y. Yamada, S.E. Park, J. Phys. Chem. C 113 (2009) 15882-15890.
[26] B.M. Reddy, L. Katta, G. Thrimurthulu, Chem. Mater. 22 (2010) 467-475.
[27] J.S. Moura, J.S.L. Fonseca, N. Bion, F. Epron, T.F. Silva, C.G. Maciel, J.M. Assaf, M.C. Rangel, Catal. Today 228 (2014) 40-50.

[28] B.M. Reddy, P. Saikia, P. Bharali, Y. Yamada, T. Kobayashi, M Muhler, W. Gruenert, J. Phys. Chem. C 112 (2008) 16393-16399.
[29] A. Martínez-Arias, A.B. Hungría, M. Fernández-García, A. Iglesias-Juez, J. Soria, J.C. Conesa, J.A. Anderson, G. Munuera, Phys. Chem. Chem. Phys. 14 (2012) 2144-2151.
[30] B.M. Reddy, G. Thrimurthulu, L. Katta, Catal. Lett. 141 (2011) 572-581.
[31] A. Trovarelli (2002) In: Hutchings GJ (ed) Catalysis by ceria and related materials, catalytic science series, vol 2. Imperial College Press, London.
[32] V. Escribano, E. López, M. Panizza, C. Resini, J. Amores, G. Busca, Solid State Sci 5 (2003) 1369–1376.
[33] J.R. McBride, K.C. Hass, B.D. Poindexter, W.H. Weber, J. Appl. Phys. 76 (1994) 2435–2441.
[34] P. Bera, K.R. Priolkar, P.R. Sarode, M.S. Hedge, S. Emura, R. Kumashiro, Chem Mater 14 (2002) 3591-3601
[35] B.M. Reddy, L. Katta, G.Thrimurthulu, Catal. Today 175 (2011) 585-592.
[36] W.Y. Hernández, O.H. Laguna, M.A. Centeno, J.A. Odriozola, J. Solid. State. Chem. 184 (2011) 3014-3020.
[37] J.E.Spanier,R.D.Robinson,F.Zhang,S.W.Chan,I.P.Herman,Phys.Rev.B64 (2001) 2454071–2454078.
[38] J.F. Yu, W. Ji, Z.S. Shen, W.S. Li, S. H. Tang, X.R. Teng, J. Raman. Spectrosc. 30 (1999) 413-415.
[39] K.M. Ryan, J.P. McGrath, R.A. Farrell. W.M. O'Neill, C.J. Barnes, M.A. Morris, J. Phys,: Condens. Matter. 15 (2003) L49-L58.
[40] F. Zhang, P. Wang, J. Koberstein, S. Khalid, S.W. Chan, Surf. Sci. 563 (2004) 74-82.
[41] R. DiMonte, J. Kaspar, J Mater Chem 15 (2005) 633-648.
[42] A. Di Benedetto, G. Landi,L. Lisi, G. Russo, Appl. Catal. B: Environ. 142 (2013) 169-177.
[43] D. Gamarra, A. Martínez-Arias, J. Catal. 263 (2009) 189-195.